Measurement of the WZ and ZZ production cross sections using leptonic final states in 8.6 fb^{-1} of pp[over ⁻] collisions

V. M. Abazov *et al.* (The D0 Collaboration)

A measurement of the WZ and ZZ production cross sections using leptonic final states in 8.6 fb^{-1} of $p\bar{p}$ collisions

V.M. Abazov,[34] B. Abbott,[72] B.S. Acharya,[28] M. Adams,[48] T. Adams,[46] G.D. Alexeev,[34] G. Alkhazov,[38]
A. Alton[a],[60] G. Alverson,[59] M. Aoki,[47] A. Askew,[46] B. Åsman,[40] S. Atkins,[57] O. Atramentov,[64] K. Augsten,[9]
C. Avila,[7] J. BackusMayes,[79] F. Badaud,[12] L. Bagby,[47] B. Baldin,[47] D.V. Bandurin,[46] S. Banerjee,[28]
E. Barberis,[59] P. Baringer,[55] J. Barreto,[3] J.F. Bartlett,[47] U. Bassler,[17] V. Bazterra,[48] A. Bean,[55] M. Begalli,[3]
C. Belanger-Champagne,[40] L. Bellantoni,[47] S.B. Beri,[26] G. Bernardi,[16] R. Bernhard,[21] I. Bertram,[41]
M. Besançon,[17] R. Beuselinck,[42] V.A. Bezzubov,[37] P.C. Bhat,[47] S. Bhatia,[62] V. Bhatnagar,[26] G. Blazey,[49]
S. Blessing,[46] K. Bloom,[63] A. Boehnlein,[47] D. Boline,[69] E.E. Boos,[36] G. Borissov,[41] T. Bose,[58] A. Brandt,[75]
O. Brandt,[22] R. Brock,[61] G. Brooijmans,[67] A. Bross,[47] D. Brown,[16] J. Brown,[16] X.B. Bu,[47] M. Buehler,[47]
V. Buescher,[23] V. Bunichev,[36] S. Burdin[b],[41] T.H. Burnett,[79] C.P. Buszello,[40] B. Calpas,[14] E. Camacho-Pérez,[31]
M.A. Carrasco-Lizarraga,[55] B.C.K. Casey,[47] H. Castilla-Valdez,[31] S. Chakrabarti,[69] D. Chakraborty,[49]
K.M. Chan,[53] A. Chandra,[77] E. Chapon,[17] G. Chen,[55] S. Chevalier-Théry,[17] D.K. Cho,[74] S.W. Cho,[30] S. Choi,[30]
B. Choudhary,[27] S. Cihangir,[47] D. Claes,[63] J. Clutter,[55] M. Cooke,[47] W.E. Cooper,[47] M. Corcoran,[77] F. Couderc,[17]
M.-C. Cousinou,[14] A. Croc,[17] D. Cutts,[74] A. Das,[44] G. Davies,[42] S.J. de Jong,[33] E. De La Cruz-Burelo,[31]
F. Déliot,[17] R. Demina,[68] D. Denisov,[47] S.P. Denisov,[37] S. Desai,[47] C. Deterre,[17] K. DeVaughan,[63] H.T. Diehl,[47]
M. Diesburg,[47] P.F. Ding,[43] A. Dominguez,[63] T. Dorland,[79] A. Dubey,[27] L.V. Dudko,[36] D. Duggan,[64]
A. Duperrin,[14] S. Dutt,[26] A. Dyshkant,[49] M. Eads,[63] D. Edmunds,[61] J. Ellison,[45] V.D. Elvira,[47] Y. Enari,[16]
H. Evans,[51] A. Evdokimov,[70] V.N. Evdokimov,[37] G. Facini,[59] T. Ferbel,[68] F. Fiedler,[23] F. Filthaut,[33] W. Fisher,[61]
H.E. Fisk,[47] M. Fortner,[49] H. Fox,[41] S. Fuess,[47] A. Garcia-Bellido,[68] G.A. García-Guerra[c],[31] V. Gavrilov,[35]
P. Gay,[12] W. Geng,[14, 61] D. Gerbaudo,[65] C.E. Gerber,[48] Y. Gershtein,[64] G. Ginther,[47, 68] G. Golovanov,[34]
A. Goussiou,[79] P.D. Grannis,[69] S. Greder,[18] H. Greenlee,[47] Z.D. Greenwood,[57] E.M. Gregores,[4] G. Grenier,[19]
Ph. Gris,[12] J.-F. Grivaz,[15] A. Grohsjean[d],[17] S. Grünendahl,[47] M.W. Grünewald,[29] T. Guillemin,[15] G. Gutierrez,[47]
P. Gutierrez,[72] A. Haas[e],[67] S. Hagopian,[46] J. Haley,[59] L. Han,[6] K. Harder,[43] A. Harel,[68] J.M. Hauptman,[54]
J. Hays,[42] T. Head,[43] T. Hebbeker,[20] D. Hedin,[49] H. Hegab,[73] A.P. Heinson,[45] U. Heintz,[74] C. Hensel,[22]
I. Heredia-De La Cruz,[31] K. Herner,[60] G. Hesketh[f],[43] M.D. Hildreth,[53] R. Hirosky,[78] T. Hoang,[46] J.D. Hobbs,[69]
B. Hoeneisen,[11] M. Hohlfeld,[23] Z. Hubacek,[9, 17] V. Hynek,[9] I. Iashvili,[66] Y. Ilchenko,[76] R. Illingworth,[47] A.S. Ito,[47]
S. Jabeen,[74] M. Jaffré,[15] D. Jamin,[14] A. Jayasinghe,[72] R. Jesik,[42] K. Johns,[44] M. Johnson,[47] A. Jonckheere,[47]
P. Jonsson,[42] J. Joshi,[26] A.W. Jung,[47] A. Juste,[39] K. Kaadze,[56] E. Kajfasz,[14] D. Karmanov,[36] P.A. Kasper,[47]
I. Katsanos,[63] R. Kehoe,[76] S. Kermiche,[14] N. Khalatyan,[47] A. Khanov,[73] A. Kharchilava,[66] Y.N. Kharzheev,[34]
J.M. Kohli,[26] A.V. Kozelov,[37] J. Kraus,[61] S. Kulikov,[37] A. Kumar,[66] A. Kupco,[10] T. Kurča,[19] V.A. Kuzmin,[36]
S. Lammers,[51] G. Landsberg,[74] P. Lebrun,[19] H.S. Lee,[30] S.W. Lee,[54] W.M. Lee,[47] J. Lellouch,[16] H. Li,[13] L. Li,[45]
Q.Z. Li,[47] S.M. Lietti,[5] J.K. Lim,[30] D. Lincoln,[47] J. Linnemann,[61] V.V. Lipaev,[37] R. Lipton,[47] Y. Liu,[6]
A. Lobodenko,[38] M. Lokajicek,[10] R. Lopes de Sa,[69] H.J. Lubatti,[79] R. Luna-Garcia[g],[31] A.L. Lyon,[47] A.K.A. Maciel,[2]
D. Mackin,[77] R. Madar,[17] R. Magaña-Villalba,[31] S. Malik,[63] V.L. Malyshev,[34] Y. Maravin,[56] J. Martínez-Ortega,[31]
R. McCarthy,[69] C.L. McGivern,[55] M.M. Meijer,[33] A. Melnitchouk,[62] D. Menezes,[49] P.G. Mercadante,[4] M. Merkin,[36]
A. Meyer,[20] J. Meyer,[22] F. Miconi,[18] N.K. Mondal,[28] G.S. Muanza,[14] M. Mulhearn,[78] E. Nagy,[14] M. Naimuddin,[27]
M. Narain,[74] R. Nayyar,[27] H.A. Neal,[60] J.P. Negret,[7] P. Neustroev,[38] S.F. Novaes,[5] T. Nunnemann,[24] G. Obrant[‡],[38]
J. Orduna,[77] N. Osman,[14] J. Osta,[53] G.J. Otero y Garzón,[1] M. Padilla,[45] A. Pal,[75] N. Parashar,[52] V. Parihar,[74]
S.K. Park,[30] R. Partridge[e],[74] N. Parua,[51] A. Patwa,[70] B. Penning,[47] M. Perfilov,[36] Y. Peters,[43] K. Petridis,[43]
G. Petrillo,[68] P. Pétroff,[15] R. Piegaia,[1] M.-A. Pleier,[70] P.L.M. Podesta-Lerma[h],[31] V.M. Podstavkov,[47] P. Polozov,[35]
A.V. Popov,[37] M. Prewitt,[77] D. Price,[51] N. Prokopenko,[37] J. Qian,[60] A. Quadt,[22] B. Quinn,[62] M.S. Rangel,[2]
K. Ranjan,[27] P.N. Ratoff,[41] I. Razumov,[37] P. Renkel,[76] M. Rijssenbeek,[69] I. Ripp-Baudot,[18] F. Rizatdinova,[73]
M. Rominsky,[47] A. Ross,[41] C. Royon,[17] P. Rubinov,[47] R. Ruchti,[53] G. Safronov,[35] G. Sajot,[13] P. Salcido,[49]
A. Sánchez-Hernández,[31] M.P. Sanders,[24] B. Sanghi,[47] A.S. Santos,[5] G. Savage,[47] L. Sawyer,[57] T. Scanlon,[42]
R.D. Schamberger,[69] Y. Scheglov,[38] H. Schellman,[50] T. Schliephake,[25] S. Schlobohm,[79] C. Schwanenberger,[43]
R. Schwienhorst,[61] J. Sekaric,[55] H. Severini,[72] E. Shabalina,[22] V. Shary,[17] A.A. Shchukin,[37] R.K. Shivpuri,[27]
V. Simak,[9] V. Sirotenko,[47] P. Skubic,[72] P. Slattery,[68] D. Smirnov,[53] K.J. Smith,[66] G.R. Snow,[63] J. Snow,[71]
S. Snyder,[70] S. Söldner-Rembold,[43] L. Sonnenschein,[20] K. Soustruznik,[8] J. Stark,[13] V. Stolin,[35] D.A. Stoyanova,[37]
M. Strauss,[72] D. Strom,[48] L. Stutte,[47] L. Suter,[43] P. Svoisky,[72] M. Takahashi,[43] A. Tanasijczuk,[1] M. Titov,[17]

V.V. Tokmenin,[34] Y.-T. Tsai,[68] K. Tschann-Grimm,[69] D. Tsybychev,[69] B. Tuchming,[17] C. Tully,[65] L. Uvarov,[38] S. Uvarov,[38] S. Uzunyan,[49] R. Van Kooten,[51] W.M. van Leeuwen,[32] N. Varelas,[48] E.W. Varnes,[44] I.A. Vasilyev,[37] P. Verdier,[19] L.S. Vertogradov,[34] M. Verzocchi,[47] M. Vesterinen,[43] D. Vilanova,[17] P. Vokac,[9] H.D. Wahl,[46] M.H.L.S. Wang,[47] J. Warchol,[53] G. Watts,[79] M. Wayne,[53] M. Weber[i],[47] J. Weichert,[23] L. Welty-Rieger,[50] A. White,[75] D. Wicke,[25] M.R.J. Williams,[41] G.W. Wilson,[55] M. Wobisch,[57] D.R. Wood,[59] T.R. Wyatt,[43] Y. Xie,[47] R. Yamada,[47] W.-C. Yang,[43] T. Yasuda,[47] Y.A. Yatsunenko,[34] W. Ye,[69] Z. Ye,[47] H. Yin,[47] K. Yip,[70] S.W. Youn,[47] T. Zhao,[79] B. Zhou,[60] J. Zhu,[60] M. Zielinski,[68] D. Zieminska,[51] and L. Zivkovic[74]

(The D0 Collaboration[*])

[1]*Universidad de Buenos Aires, Buenos Aires, Argentina*
[2]*LAFEX, Centro Brasileiro de Pesquisas Físicas, Rio de Janeiro, Brazil*
[3]*Universidade do Estado do Rio de Janeiro, Rio de Janeiro, Brazil*
[4]*Universidade Federal do ABC, Santo André, Brazil*
[5]*Instituto de Física Teórica, Universidade Estadual Paulista, São Paulo, Brazil*
[6]*University of Science and Technology of China, Hefei, People's Republic of China*
[7]*Universidad de los Andes, Bogotá, Colombia*
[8]*Charles University, Faculty of Mathematics and Physics, Center for Particle Physics, Prague, Czech Republic*
[9]*Czech Technical University in Prague, Prague, Czech Republic*
[10]*Center for Particle Physics, Institute of Physics, Academy of Sciences of the Czech Republic, Prague, Czech Republic*
[11]*Universidad San Francisco de Quito, Quito, Ecuador*
[12]*LPC, Université Blaise Pascal, CNRS/IN2P3, Clermont, France*
[13]*LPSC, Université Joseph Fourier Grenoble 1, CNRS/IN2P3, Institut National Polytechnique de Grenoble, Grenoble, France*
[14]*CPPM, Aix-Marseille Université, CNRS/IN2P3, Marseille, France*
[15]*LAL, Université Paris-Sud, CNRS/IN2P3, Orsay, France*
[16]*LPNHE, Universités Paris VI and VII, CNRS/IN2P3, Paris, France*
[17]*CEA, Irfu, SPP, Saclay, France*
[18]*IPHC, Université de Strasbourg, CNRS/IN2P3, Strasbourg, France*
[19]*IPNL, Université Lyon 1, CNRS/IN2P3, Villeurbanne, France and Université de Lyon, Lyon, France*
[20]*III. Physikalisches Institut A, RWTH Aachen University, Aachen, Germany*
[21]*Physikalisches Institut, Universität Freiburg, Freiburg, Germany*
[22]*II. Physikalisches Institut, Georg-August-Universität Göttingen, Göttingen, Germany*
[23]*Institut für Physik, Universität Mainz, Mainz, Germany*
[24]*Ludwig-Maximilians-Universität München, München, Germany*
[25]*Fachbereich Physik, Bergische Universität Wuppertal, Wuppertal, Germany*
[26]*Panjab University, Chandigarh, India*
[27]*Delhi University, Delhi, India*
[28]*Tata Institute of Fundamental Research, Mumbai, India*
[29]*University College Dublin, Dublin, Ireland*
[30]*Korea Detector Laboratory, Korea University, Seoul, Korea*
[31]*CINVESTAV, Mexico City, Mexico*
[32]*Nikhef, Science Park, Amsterdam, the Netherlands*
[33]*Radboud University Nijmegen, Nijmegen, the Netherlands and Nikhef, Science Park, Amsterdam, the Netherlands*
[34]*Joint Institute for Nuclear Research, Dubna, Russia*
[35]*Institute for Theoretical and Experimental Physics, Moscow, Russia*
[36]*Moscow State University, Moscow, Russia*
[37]*Institute for High Energy Physics, Protvino, Russia*
[38]*Petersburg Nuclear Physics Institute, St. Petersburg, Russia*
[39]*Institució Catalana de Recerca i Estudis Avançats (ICREA) and Institut de Física d'Altes Energies (IFAE), Barcelona, Spain*
[40]*Stockholm University, Stockholm and Uppsala University, Uppsala, Sweden*
[41]*Lancaster University, Lancaster LA1 4YB, United Kingdom*
[42]*Imperial College London, London SW7 2AZ, United Kingdom*
[43]*The University of Manchester, Manchester M13 9PL, United Kingdom*
[44]*University of Arizona, Tucson, Arizona 85721, USA*
[45]*University of California Riverside, Riverside, California 92521, USA*
[46]*Florida State University, Tallahassee, Florida 32306, USA*
[47]*Fermi National Accelerator Laboratory, Batavia, Illinois 60510, USA*
[48]*University of Illinois at Chicago, Chicago, Illinois 60607, USA*
[49]*Northern Illinois University, DeKalb, Illinois 60115, USA*
[50]*Northwestern University, Evanston, Illinois 60208, USA*
[51]*Indiana University, Bloomington, Indiana 47405, USA*

[52] *Purdue University Calumet, Hammond, Indiana 46323, USA*
[53] *University of Notre Dame, Notre Dame, Indiana 46556, USA*
[54] *Iowa State University, Ames, Iowa 50011, USA*
[55] *University of Kansas, Lawrence, Kansas 66045, USA*
[56] *Kansas State University, Manhattan, Kansas 66506, USA*
[57] *Louisiana Tech University, Ruston, Louisiana 71272, USA*
[58] *Boston University, Boston, Massachusetts 02215, USA*
[59] *Northeastern University, Boston, Massachusetts 02115, USA*
[60] *University of Michigan, Ann Arbor, Michigan 48109, USA*
[61] *Michigan State University, East Lansing, Michigan 48824, USA*
[62] *University of Mississippi, University, Mississippi 38677, USA*
[63] *University of Nebraska, Lincoln, Nebraska 68588, USA*
[64] *Rutgers University, Piscataway, New Jersey 08855, USA*
[65] *Princeton University, Princeton, New Jersey 08544, USA*
[66] *State University of New York, Buffalo, New York 14260, USA*
[67] *Columbia University, New York, New York 10027, USA*
[68] *University of Rochester, Rochester, New York 14627, USA*
[69] *State University of New York, Stony Brook, New York 11794, USA*
[70] *Brookhaven National Laboratory, Upton, New York 11973, USA*
[71] *Langston University, Langston, Oklahoma 73050, USA*
[72] *University of Oklahoma, Norman, Oklahoma 73019, USA*
[73] *Oklahoma State University, Stillwater, Oklahoma 74078, USA*
[74] *Brown University, Providence, Rhode Island 02912, USA*
[75] *University of Texas, Arlington, Texas 76019, USA*
[76] *Southern Methodist University, Dallas, Texas 75275, USA*
[77] *Rice University, Houston, Texas 77005, USA*
[78] *University of Virginia, Charlottesville, Virginia 22901, USA*
[79] *University of Washington, Seattle, Washington 98195, USA*

We study the processes $p\bar{p} \to WZ \to \ell^{\pm}\nu\ell^{+}\ell^{-}$ and $p\bar{p} \to ZZ \to \ell^{+}\ell^{-}\nu\bar{\nu}$, where $\ell = e$ or μ. Using 8.6 fb^{-1} of integrated luminosity collected by the D0 experiment at the Fermilab Tevatron collider, we measure the WZ production cross section to be $4.50^{+0.63}_{-0.66}$ pb which is consistent with, but slightly larger than the prediction of the standard model. The ZZ cross section is measured to be 1.64 ± 0.46 pb, in agreement with a prediction of the standard model. Combination with an earlier analysis of the $ZZ \to \ell^{+}\ell^{-}\ell^{+}\ell^{-}$ channel yields a ZZ cross section of $1.44^{+0.35}_{-0.34}$ pb.

I. INTRODUCTION

This Article reports a study of $WZ \to \ell^{\pm}\nu\ell^{+}\ell^{-}$ and $ZZ \to \ell^{+}\ell^{-}\nu\bar{\nu}$ production in $p\bar{p}$ collisions at a center-of-mass energy of $\sqrt{s} = 1.96$ TeV. When not stated otherwise, we denote as Z the full Z/γ^* propagator, with the requirement of $60 < M_{\ell\ell} < 120$ GeV on the dilepton invariant mass $M_{\ell\ell}$ for the decay $Z \to \ell^{+}\ell^{-}$.

The pair production of W and Z gauge bosons probes the electroweak component of the standard model (SM) as these cross sections are predicted to be significantly larger in the presence of new resonances or anomalous triple-gauge-couplings [1, 2]. Diboson production is a major source of background in many search channels for

Higgs bosons. For example, ZZ decays correspond to some of the dominant backgrounds in searches for ZH production at the Tevatron. Understanding diboson production is therefore crucial for demonstrating sensitivity to the presence of a SM Higgs boson at the Tevatron.

Production of WZ was first reported by the CDF Collaboration, in 1.1 fb^{-1} of integrated luminosity in the $\ell^{\pm}\nu\ell^{+}\ell^{-}$ channel [3]. Evidence for $WZ \to \ell^{\pm}\nu\ell^{+}\ell^{-}$ production was also presented by the D0 Collaboration in 1.0 fb^{-1} of integrated luminosity [4]. The D0 Collaboration studied the same process with 4.1 fb^{-1} [5], measuring a production cross section of $3.90^{+1.06}_{-0.90}$ pb. The production of ZZ in hadron collisions was first observed by D0 in the $\ell^{+}\ell^{-}\ell^{+}\ell^{-}$ final state with 2.7 fb^{-1} [6]. Combination with an analysis of the $\ell^{+}\ell^{-}\nu\bar{\nu}$ final state with 2.7 fb^{-1} [7], increased the significance from 5.3 to 5.7 standard deviations [6]. Evidence for ZZ production was also presented by CDF in 1.9 fb^{-1} [8] of integrated luminosity. D0 has recently analyzed 6.4 fb^{-1} of integrated luminosity in the $\ell^{+}\ell^{-}\ell^{+}\ell^{-}$ final state [9]. Combination with the earlier 2.7 fb^{-1} analysis [7] of the $\ell^{+}\ell^{-}\nu\bar{\nu}$ final state yielded a ZZ production cross section of $1.40^{+0.43}_{-0.37}(\text{stat}) \pm 0.14(\text{syst})$ pb [10]. The CDF Collabora-

---
[*] with visitors from [a] Augustana College, Sioux Falls, SD, USA, [b] The University of Liverpool, Liverpool, UK, [c] UPIITA-IPN, Mexico City, Mexico, [d] DESY, Hamburg, Germany, [e] SLAC, Menlo Park, CA, USA, [f] University College London, London, UK, [g] Centro de Investigacion en Computacion - IPN, Mexico City, Mexico, [h] ECFM, Universidad Autonoma de Sinaloa, Culiacán, Mexico, and [i] Universität Bern, Bern, Switzerland. [‡] Deceased.

tion recently measured a cross section of $1.64^{+0.44}_{-0.38}$ pb for ZZ production using 6 fb^{-1} in the $\ell^+\ell^-\ell^+\ell^-$ and $\ell^+\ell^-\nu\bar{\nu}$ final states [11]. The ATLAS Collaboration has recently studied the $WZ \to \ell^{\pm}\nu\ell^+\ell^-$ and $ZZ \to \ell^+\ell^-\ell^+\ell^-$ processes in pp collisions at $\sqrt{s} = 7$ TeV using 1.1 fb^{-1} of integrated luminosity [12, 13].

Following the approach of the previous D0 analysis [7] of the $ZZ \to \ell^+\ell^-\nu\bar{\nu}$ signal, we measure the ratios of signal cross sections relative to the inclusive Z boson cross section. This has the advantage of canceling the uncertainty on the luminosity, while other systematic uncertainties related to lepton identification and trigger efficiencies, are also largely canceled.

All selection requirements and analysis techniques are optimized based on Monte Carlo (MC) simulation, or on data in signal-free control regions. The data are examined in the region expected for signal only after all selection criteria are defined through simulation.

II. APPARATUS

The D0 detector [14–16] has a central-tracking system, consisting of a silicon microstrip tracker (SMT) and a central fiber tracker (CFT), both located within a 1.9 T superconducting solenoidal magnet, with designs optimized for tracking and vertexing at pseudorapidities [17] $|\eta| < 3$ and $|\eta| < 2.5$, respectively. A liquid-argon and uranium calorimeter has a central section (CC) covering $|\eta|$ up to ≈ 1.1 and two end calorimeters (EC) that extend coverage to $|\eta| \approx 4.2$, with all three housed in separate cryostats. The inter-cryostat (IC) region (1.1 $< |\eta| < 1.5$) has little electromagnetic (EM) calorimetry, and reduced hadronic coverage. Additional scintillating tiles covering the region $1.1 < |\eta| < 1.4$ provide improved energy resolution for hadronic jets. An outer muon system, covering $|\eta| < 2$, consists of a layer of wire chambers and scintillation trigger counters in front of 1.8 T toroidal magnets, followed by two similar layers after the toroids.

III. DATA AND INITIAL EVENT SELECTION

The data used in this analysis were collected with the D0 detector at the Fermilab Tevatron $p\bar{p}$ collider at a center-of-mass energy of $\sqrt{s} = 1.96$ TeV. An integrated luminosity of 8.6 fb^{-1} is available for analysis, following application of data quality requirements.

Unlike the previous D0 analyses of these channels, we do not restrict the offline event selection to events satisfying specific trigger conditions. Rather, we analyse all recorded data in order to maximise the event yields. The analyzed events are mostly recorded by triggers that require one or two electrons or muons with high transverse momentum, p_T.

Since both signal processes involve the decay $Z \to \ell^+\ell^-$, a natural starting point is to select an inclusive sample of dilepton events. In addition to the e^+e^-

and $\mu^+\mu^-$ dilepton channels, the ZZ analysis makes extensive use of the $e^{\pm}\mu^{\mp}$ channel for verifying modeling of dominant backgrounds (mostly $WW \to \ell^+\nu\ell^-\bar{\nu}$). In all channels we require that there are two oppositely charged leptons with an invariant mass $M_{\ell\ell}$ between 60 and 120 GeV. The regions $40 < M_{\ell\ell} < 60$ GeV and $M_{\ell\ell} > 120$ GeV are used as control regions. The two leptons are required to originate from a common vertex that is located within $\pm$ 80 cm of the detector center along the z axis, defined by the beam direction. This requirement is more than 99% efficient, which is verified to be sufficiently well modeled in the simulation.

We define three different qualities for electrons and muons and refer to electrons or muons satisfying the corresponding selection criteria, discussed below, as loose, medium, and tight, respectively. Electrons are treated differently when they are reconstructed in the CC, EC, and IC regions of the calorimeter. Loose CC/EC electron candidates are reconstructed using EM energy clusters in the calorimeter that satisfy minimal shower shape and isolation requirements and that are spatially matched to central tracks. A boosted decision tree (BDT) [18] is trained to separate electrons from jets, based on tracking, isolation, and shower shape information. Medium and tight CC/EC electrons must satisfy increasingly stringent requirements on the output from this BDT.

In the IC region, there is no dedicated reconstruction of electrons. However, electrons traversing this region are identified using an algorithm that searches for hadronic decays of tau leptons. A neural network is trained to use shower shape, isolation, and tracking information to recover electrons from reconstructed taus while rejecting hadronic jets. Electrons found in the IC region must be matched to a central track with at least one hit in the SMT and ten hits in the CFT. Loose, medium, and tight IC electrons must satisfy increasingly stringent requirements on the neural network output. In addition, medium(tight) IC electrons must satisfy $\mathcal{I}^{\text{elec}}_{\text{trk}}/p_T < 0.2(0.1)$, where $\mathcal{I}^{\text{elec}}_{\text{trk}}$ is the scalar p_T sum of all tracks within an annulus of radius $0.05 < \Delta\mathcal{R} < 0.4$ [19] around the candidate electron. All reconstructed tracks with $p_T > 0.5$ GeV are included in this sum. IC electrons are placed into two sub-categories: type-2(1) IC electrons do (not) contain a cluster of energy in the EM layers of the calorimeter. For type-2 IC electrons the momentum is determined from the calorimeter energy, whereas for type-1 IC electrons, we rely on the central track, which provides a relatively poor momentum resolution.

Loose muons are required to have a track segment that has wire and scintillator hits in at least one layer of the muon spectrometer and a spatially matched track in the central detector. Loose muons must also satisfy a calorimeter isolation requirement of $\mathcal{I}^{\text{muon}}_{\text{cal}}/p_T < 0.4$, where $\mathcal{I}^{\text{muon}}_{\text{cal}}$ is the scalar sum of transverse energies of all calorimeter cells within an annulus of radius $0.1 < \Delta\mathcal{R} < 0.4$ around the candidate muon. A track isolation requirement, $\mathcal{I}^{\text{muon}}_{\text{trk}}/p_T < 0.4$, is also imposed on loose muons, where $\mathcal{I}^{\text{muon}}_{\text{trk}}$ is the scalar p_T sum of

all tracks within a cone of radius $\Delta\mathcal{R} < 0.5$ relative to the candidate muon. Medium(tight) muons must satisfy $\mathcal{I}_{\text{cal}}^{\text{muon}}/p_T < 0.2(0.1)$ and $\mathcal{I}_{\text{trk}}^{\text{muon}}/p_T < 0.2(0.1)$.

The number of events that pass an inclusive dilepton selection is used as the denominator for the purposes of measuring the ratio of WZ and ZZ cross sections to the Z cross section. The WZ dilepton selection requires two opposite charge medium quality leptons of the same flavor. Hard and soft electron(muon) p_T requirements are defined as $p_T > 20(15)$ GeV and $p_T > 15(10)$ GeV, respectively. IC electrons are considered only if they satisfy $p_T > 20$ GeV. The e^+e^- and $\mu^+\mu^-$ channels require that both leptons satisfy the appropriate soft p_T requirement, and that at least one lepton satisfies the appropriate hard p_T requirement.

The ZZ dilepton selection requires tight rather than medium leptons, and also includes the $e^\pm\mu^\mp$ control channel. The lepton p_T requirements are the same as in the WZ analysis. Since a reliable energy/momentum measurement is needed to suppress background from mis-reconstructed $Z \to \ell^+\ell^-$ events, type-1 IC electrons are excluded. In the $e^\pm\mu^\mp$ channel, electrons are considered only in the CC and EC regions. Figure 1 compares the $M_{\ell\ell}$ distribution in data and simulation (described in Section IV) after the ZZ dilepton selection, prior to any additional requirements. The data are well described by the simulation apart from the region of large $M_{\ell\ell}$ in the dielectron channel where the simulation yields more events than the data due to a mis-modeling of the resolution tails. This is shown not to have a significant effect on the analysis. In the $e^\pm\mu^\mp$ channel, the well modeled shoulder around $M_{\ell\ell} \approx 90$ GeV is due to $Z \to \mu^+\mu^-$ events in which a muon looses a significant amount of energy in the electromagnetic calorimeter and is mis-reconstructed as an electron.

The $Z \to \ell^+\ell^-$ selections used as denominators in the cross section ratio measurements include some further requirements that are detailed in Sections V and VII.

IV. PREDICTION FOR BACKGROUND AND SIGNAL

Background yields are estimated using a combination of control data samples and MC simulation. The signal processes and certain backgrounds ($WW \to \ell^+\nu\ell^-\bar{\nu}$, $ZZ \to \ell^+\ell^-\ell^+\ell^-$, $Z \to \ell^+\ell^-$, $t\bar{t} \to \ell^+\ell^-\nu\bar{\nu}b\bar{b}$, $Z\gamma \to \ell^+\ell^-\gamma$ and $W\gamma \to \ell^\pm\nu\gamma$) are estimated based on simulations using the PYTHIA [20] event generator and leading order CTEQ6L1 [21] parton distribution functions (PDF). Events are passed through a GEANT [22] based simulation of the D0 detector response. In addition, randomly triggered bunch crossings from data are added to the simulated events to model the effect of additional $p\bar{p}$ collisions. The GEANT based simulation does not include efficiency of the trigger. Instead, the efficiencies of certain triggers (single-electron and single-muon) are measured using $Z \to \ell^+\ell^-$ candi-

date events from data. A parameterization of these efficiencies is applied to the simulated events, with a correction determined from data for the additional efficiency that is gained from the remaining triggers (mostly dilepton and lepton-plus-jet triggers). The MC simulation does not accurately describe the dilepton p_T distribution in Z production. Weights are therefore assigned to the simulated events as a function of their generated dilepton p_T, based on a comparison with more accurate predictions from RESBOS [23]. The diboson events are similarly corrected as a function of diboson p_T to match predictions from the next-to-leading order (NLO) event generator POWHEG [24, 25]. The simulation of WZ production by PYTHIA does not include diagrams with $\gamma^* \to \ell^+\ell^-$. Weights are assigned to the generated events based on comparison of the $Z \to \ell^+\ell^-$ invariant mass distribution with POWHEG, which does include these diagrams. The simulated events are further corrected for inaccuracies in reconstruction efficiency and energy/momentum resolution for leptons. The MC predictions are normalized to match the observed event yield after the inclusive dilepton selection, such that knowledge of the integrated luminosity is not required.

Instrumental backgrounds arise from the mis-reconstruction of hadronic jets as isolated electron and muon candidates. These backgrounds are estimated from data using the so-called "Matrix Method" [26], since their rates cannot be modeled sufficiently well by the MC. We select a sample of events in which a high p_T jet satisfies the trigger conditions for the event and is back-to-back in ϕ with an electron or muon that satisfies the loose requirements. We measure the efficiency (ϵ_{jet}) for a jet that is mis-reconstructed as a loose lepton to also satisfy the medium or tight lepton requirements. The equivalent efficiency for genuine electrons and muons (ϵ_{sig}) is measured in a sample of $Z \to \ell^+\ell^-$ candidate events. The Z+jets background in the $WZ \to \ell^\pm\nu\ell^+\ell^-$ sample is estimated by selecting a sample of events in which the lepton assigned to the $W \to \ell\nu$ decay is of loose rather than tight quality. Given the estimates of ϵ_{sig} and ϵ_{jet}, we solve a set of simultaneous equations to estimate the amount of background in the tight sample. A sample of Z+jets events generated with PYTHIA is normalized to the estimate from data. The W+jets background in the $ZZ \to \ell^+\ell^-\nu\bar{\nu}$ sample is estimated in a similar way, with a sample of MC events normalized to an estimate from data. In the inclusive dilepton sample, there is a small background from multijet events in the e^+e^- channel. This background is estimated by fitting the observed $M_{\ell\ell}$ distribution with the sum of simulated contributions and a multijet template that is obtained by inverting the electron quality cuts in real data. A study of events in which the two leptons have the same charge indicates that the multijet background is negligible in the $\mu^+\mu^-$ channel.
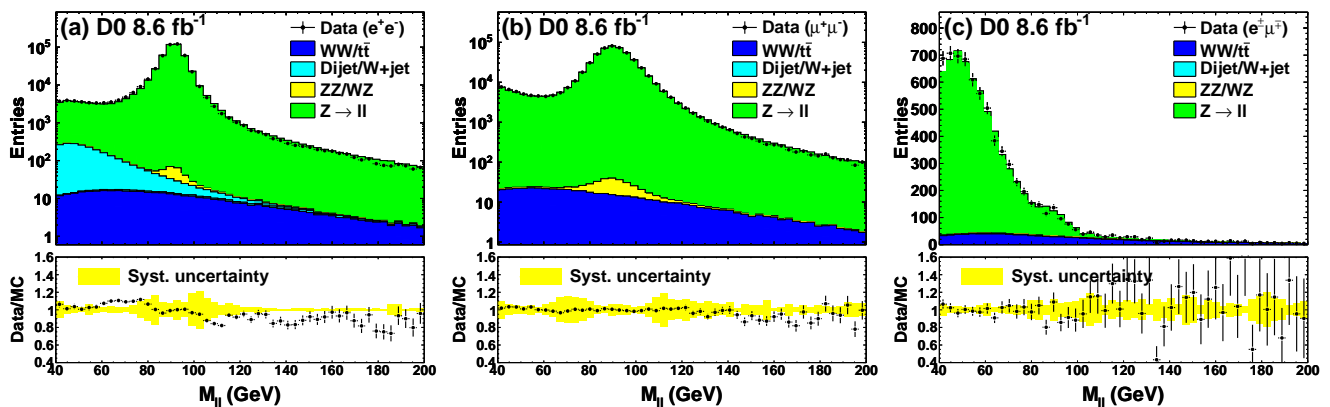
FIG. 1: Comparison of data and simulation in the $M_{\ell\ell}$ distribution after selecting an oppositely charged pair of tight quality leptons in the (a) e^+e^-, (b) $\mu^+\mu^-$, and (c) $e^\pm\mu^\mp$ channels. The lower halves of the plots show the ratio of data to simulation, with the yellow band representing the systematic uncertainty (see Section VIII) on the simulation.

V. SELECTION OF WZ CANDIDATES

Four channels are considered for WZ decay: $e^+e^-e^\pm$, $e^+e^-\mu^\pm$, $\mu^+\mu^-e^\pm$, $\mu^+\mu^-\mu^\pm$. Events must contain two oppositely charged medium quality leptons satisfying the p_T requirements described earlier and with $M_{\ell\ell}$ between 60 and 120 GeV. The selection of WZ candidates further requires an additional electron (CC or EC) or muon with $p_T > 15$ GeV, and tight quality. This lepton must originate from a common vertex with the lepton pair that is assigned to the $Z \to \ell^+\ell^-$ decay. If there are three like flavor leptons, there are two possible combinations of opposite charge leptons. In this case, the pair with smallest $|M_{\ell\ell} - m_Z|$, where m_Z is the Z boson mass [27], is assigned to the $Z \to \ell^+\ell^-$ decay. Simulation shows that this assignment is correct in 93% of cases in the three electron channel, and 87% of cases in the three muon channel. In order to suppress the contribution from $ZZ \to \ell^+\ell^-\ell^+\ell^-$ decays, no additional reconstructed EM clusters are allowed for the $\ell^+\ell^-e^\pm$ selection, and no additional reconstructed muons for the $\ell^+\ell^-\mu^\pm$ selection. The additional EM clusters must satisfy $E_T > 5$ GeV. Clusters that are not matched to a central track must satisfy loose shower shape requirements. There are no explicit p_T or isolation requirements imposed on the additional muons. Events that satisfy these requirements, excluding the requirement of a third lepton, are considered as Z candidates, to be used in the denominator when measuring the ratio of WZ and Z cross sections. We choose to include a veto on more than two leptons in the Z selection, such that uncertainties in the veto efficiency are mostly cancelled in the ratio of WZ to Z cross sections.

The WZ events are characterised by large missing transverse energy, $\not{E}_T$, defined as the magnitude of a vector sum of the transverse energies of cells in the calorimeter. The $\not{E}_T$ is corrected for muons, which only deposit a small fraction of their energy in the calorimeter, and for the energy loss of electrons. The variable $\not{E}_T'$ is defined

by recalculating the $\not{E}_T$ after rescaling the transverse momenta of the leptons that are assigned to be Z daughters within 3 standard deviations of their resolution $\sigma(p_T^{(i)})$, through a fit that minimises the χ^2 function:

$$\chi^2 = \left(\frac{M_{\ell\ell} - m_Z}{\Gamma_Z}\right)^2 + \left(\frac{\delta p_T^{(1)}}{\sigma(p_T^{(1)})}\right)^2 + \left(\frac{\delta p_T^{(2)}}{\sigma(p_T^{(2)})}\right)^2, \quad (1)$$

where Γ_Z is the total width of the Z boson [27], and $\delta p_T^{(i)}$ is the amount by which the p_T of lepton i is shifted. This kinematic constraint is only used for the purposes of calculating the variable $\not{E}_T'$. The requirement of $\not{E}_T' > 20$ GeV is imposed in order to reject Z+jets and $Z\gamma$ backgrounds. A background to the sub-channels with a $W \to e\nu$ decay is the radiation of a high p_T photon from a lepton in a $Z \to \ell^+\ell^-$ decay. We therefore require that $|M_{\ell\ell\ell} - 91.2| > |M_{\ell\ell} - 91.2|$, where $M_{\ell\ell\ell}$ is the invariant mass of the three leptons. In addition, at least one of the leptons from the $Z \to \ell^+\ell^-$ decay is required to have $p_T > 25$ GeV.

Tables I and II list the observed and predicted event yields after all WZ selection requirements. The yields are also listed for the samples that exclusively fail the $\not{E}_T$ or $M_{\ell\ell}$ requirements, but satisfy all other requirements. Figure 2 shows the $\not{E}_T$, $M_{\ell\ell}$, and M_T^W distributions for $WZ \to \ell^\pm\nu\ell^+\ell^-$ candidate events, before imposing the requirement on each variable. The transverse mass is defined as $M_T^W = \sqrt{2p_T \not{E}_T(1 - \cos\Delta\phi)}$, with p_T being the transverse momentum of the charged lepton that is assigned as the W daughter, and $\Delta\phi$ being the azimuthal angle between this lepton and the $\not{E}_T$ vector. Figure 3 shows the distributions of various kinematic quantities after combining the four sub-channels.

TABLE I: $WZ \to \ell^{\pm}\nu\ell^+\ell^-$ selection: Predicted and observed yields in the $Z \to e^+e^-$ sub-channels. The systematic uncertainties are provided for the predictions.

	$e^+e^-e^{\pm}$ channel			$e^+e^-\mu^{\pm}$ channel		
	Accepted	fail $\not{E}_T$	fail $M_{\ell\ell}$	Accepted	fail $\not{E}_T$	fail $M_{\ell\ell}$
$Z \to \ell^+\ell^-$	0.3 ± 0.1	9 ± 1	–	3 ± 1	7 ± 2	0.1 ± 0.0
$Z\gamma \to \ell^+\ell^-\gamma$	0.6 ± 0.2	10.1 ± 0.6	–	0.1 ± 0.0	0.1 ± 0.0	–
$ZZ \to \ell^+\ell^-\ell^+\ell^-$	0.6 ± 0.1	1.0 ± 0.1	–	1.5 ± 0.0	0.7 ± 0.0	0.1 ± 0.0
$t\bar{t} \to \ell^+\ell^-\nu\bar{\nu}b\bar{b}$	–	–	–	–	–	–
Predicted background	1.5 ± 0.4	20 ± 1	0.1 ± 0.0	5 ± 1	7 ± 2	0.2 ± 0.1
$WZ \to \ell^{\pm}\nu\ell^+\ell^-$	9.9 ± 0.2	1.7 ± 0.1	0.1 ± 0.1	13.9 ± 0.3	2.2 ± 0.1	0.6 ± 0.1
Predicted total	11.4 ± 0.4	21 ± 1	0.2 ± 0.1	19 ± 1	9 ± 2	0.8 ± 0.2
Observed	17	32	0	17	6	1

TABLE II: $WZ \to \ell^{\pm}\nu\ell^+\ell^-$ selection: Predicted and observed yields in the $Z \to \mu^+\mu^-$ sub-channels. The systematic uncertainties are provided for the predictions.

	$\mu^+\mu^-e^{\pm}$ channel			$\mu^+\mu^-\mu^{\pm}$ channel		
	Accepted	fail $\not{E}_T$	fail $M_{\ell\ell}$	Accepted	fail $\not{E}_T$	fail $M_{\ell\ell}$
$Z \to \ell^+\ell^-$	1.5 ± 0.4	12 ± 2	0.5 ± 0.2	4 ± 2	3 ± 1	0.1 ± 0.5
$Z\gamma \to \ell^+\ell^-\gamma$	1.6 ± 0.4	13.0 ± 0.5	0.3 ± 0.1	0.1 ± 0.0	0.1 ± 0.0	–
$ZZ \to \ell^+\ell^-\ell^+\ell^-$	0.9 ± 0.2	1.5 ± 0.2	0.1 ± 0.0	1.6 ± 0.0	0.7 ± 0.0	0.1 ± 0.0
$t\bar{t} \to \ell^+\ell^-\nu\bar{\nu}b\bar{b}$	0.3 ± 0.0	–	0.1 ± 0.0	0.1 ± 0.0	–	–
Predicted background	4.3 ± 0.8	26 ± 2	1.0 ± 0.3	6 ± 2	4 ± 1	0.2 ± 0.5
$WZ \to \ell^{\pm}\nu\ell^+\ell^-$	14.0 ± 0.2	2.1 ± 0.1	0.9 ± 0.1	15.1 ± 0.4	2.0 ± 0.1	0.3 ± 0.1
Predicted total	18.3 ± 0.8	29 ± 2	1.9 ± 0.4	21 ± 2	6 ± 1	0.5 ± 0.6
Observed	26	23	3	25	12	5

VI. MISSING TRANSVERSE MOMENTUM ESTIMATORS

The basic signature for the $ZZ \to \ell^+\ell^-\nu\bar{\nu}$ analysis is a pair of charged leptons with invariant mass close to m_Z, produced in association with significant imbalance in transverse momentum, $\not{p}_T$, due to the neutrinos from the $Z \to \nu\bar{\nu}$ decay. A substantial background corresponds to inclusive $Z \to \ell^+\ell^-$ production in which either the leptons and/or any hadronic recoil is mis-reconstructed. Stringent selection requirements are necessary to suppress this background, since (i) the production cross section for Z bosons exceeds that of the signal by four orders of magnitude and (ii) the rates for mis-reconstruction are difficult to simulate. Rather than estimate the genuine $\not{p}_T$ in the event, we use the approach of the previous D0 analysis of this process [7], and construct variables that represent the minimum $\not{p}_T$ consistent with the measurement uncertainties on the leptons and the hadronic recoil.

First, the dilepton $\vec{p}_T$ is decomposed into two components with respect to a reference axis, $\vec{t}$, as illustrated in Fig. 4. We define $\vec{t} = \vec{p}_T^{(1)} - \vec{p}_T^{(2)}$, where $\vec{p}_T^{(1)}$ and $\vec{p}_T^{(2)}$ are the p_T vectors of the two leptons. The dilepton p_T vector is defined as $\vec{p}_T = \vec{p}_T^{(1)} + \vec{p}_T^{(2)}$, from which we define

$$p_T^{\ell\ell} = |\vec{p_T}|, \qquad (2)$$
$$a_T^{\ell\ell} = |\vec{p_T} \times \hat{t}|, \qquad (3)$$
$$a_L^{\ell\ell} = |\vec{p_T} \cdot \hat{t}|, \qquad (4)$$

where $\hat{t}$ is a unit vector in the direction of $\vec{t}$. In the region $\Delta\phi > \pi/2$, where $\Delta\phi$ is the azimuthal opening angle between the leptons, the $a_T^{\ell\ell}$ component is less sensitive to mis-measurement in the magnitude of the individual lepton transverse momenta than is $a_L^{\ell\ell}$ [7, 28]. For $\Delta\phi < \pi/2$, this decomposition is no longer valid, and $a_T^{\ell\ell}$ and $a_L^{\ell\ell}$ are set equal to $p_T^{\ell\ell}$.

The missing transverse momentum estimators, $\not{p}'_T$, $\not{a}'_T$, and $\not{a}'_L$, are constructed as

$$\not{p}'_T = p_T^{\ell\ell} + 2\left[p_T^{\delta} + p_T^{\text{recoil}} + p_T^{\text{trkjets}}\right], \qquad (5)$$
$$\not{a}'_T = a_T^{\ell\ell} + 2\left[a_T^{\delta} + a_T^{\text{recoil}} + a_T^{\text{trkjets}}\right], \qquad (6)$$
$$\not{a}'_L = a_L^{\ell\ell} + 2\left[a_L^{\delta} + a_L^{\text{recoil}} + a_L^{\text{trkjets}}\right]. \qquad (7)$$

The terms, p_T^{δ}, p_T^{recoil} and p_T^{trkjets} (and similarly for a_T and a_L) are corrections for lepton p_T mis-measurement, hadronic recoil measured in the calorimeter, and remaining hadronic recoil measured in the tracking system, respectively. These terms are described in more detail in
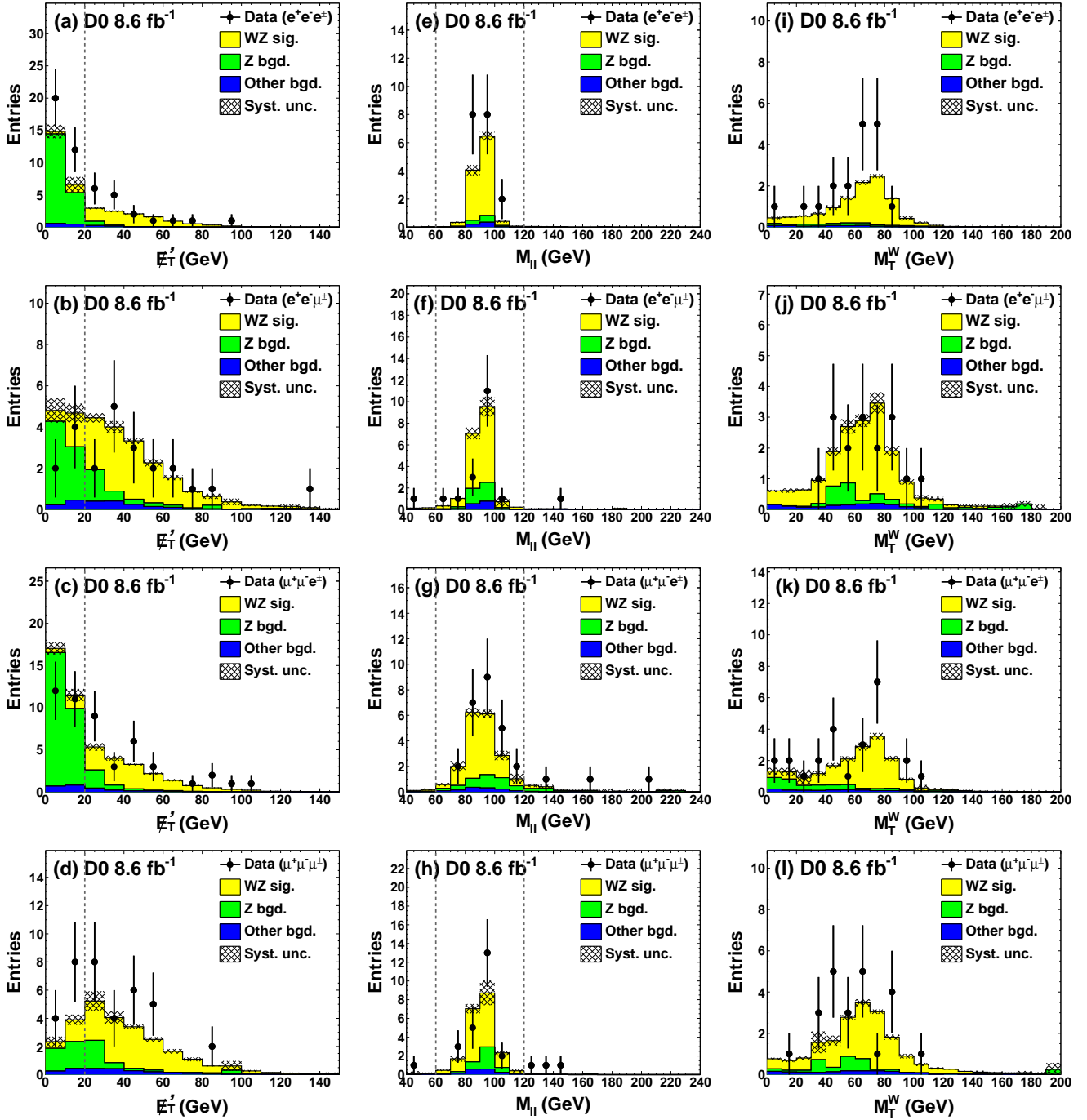
FIG. 2: The distribution of (a-d) $\not{E}'_T$, (e-h) $M_{\ell\ell}$ and (i-l) the W transverse mass of the WZ candidate events. The $\not{E}'_T$ requirement is not imposed for (a-d), and the $M_{\ell\ell}$ requirement is not imposed for (e-h). The rows correspond to different sub-channels as indicated on the figures. The vertical dashed lines indicate the requirements on $\not{E}'_T$ and $M_{\ell\ell}$. The signal normalization is as described in Section IV.

the following sections. The factor of two is found to be optimal based on MC simulations.

A. Dilepton mis-measurement

A correction for possible lepton p_T mis-measurement is determined by varying each individual lepton p_T within one standard deviation of its estimated uncertainty in order to separately minimise $a_T^{\ell\ell}$, $a_L^{\ell\ell}$ and $p_T^{\ell\ell}$. Electrons

FIG. 3: Kinematic distributions for the $WZ \to \ell^{\pm}\nu\ell^{+}\ell^{-}$ signal candidates after combining the different sub-channels. The following variables are shown: (a) the $\not{E}_T'$; (b) the invariant mass of the $Z \to \ell^{+}\ell^{-}$ decay; (c) the W transverse mass; the transverse momenta of the (d) leading and (e) subleading leptons from the $Z \to \ell^{+}\ell^{-}$ decay and (f) the charged lepton from the W decay; the transverse momenta of the reconstructed (g) $Z \to \ell^{+}\ell^{-}$ and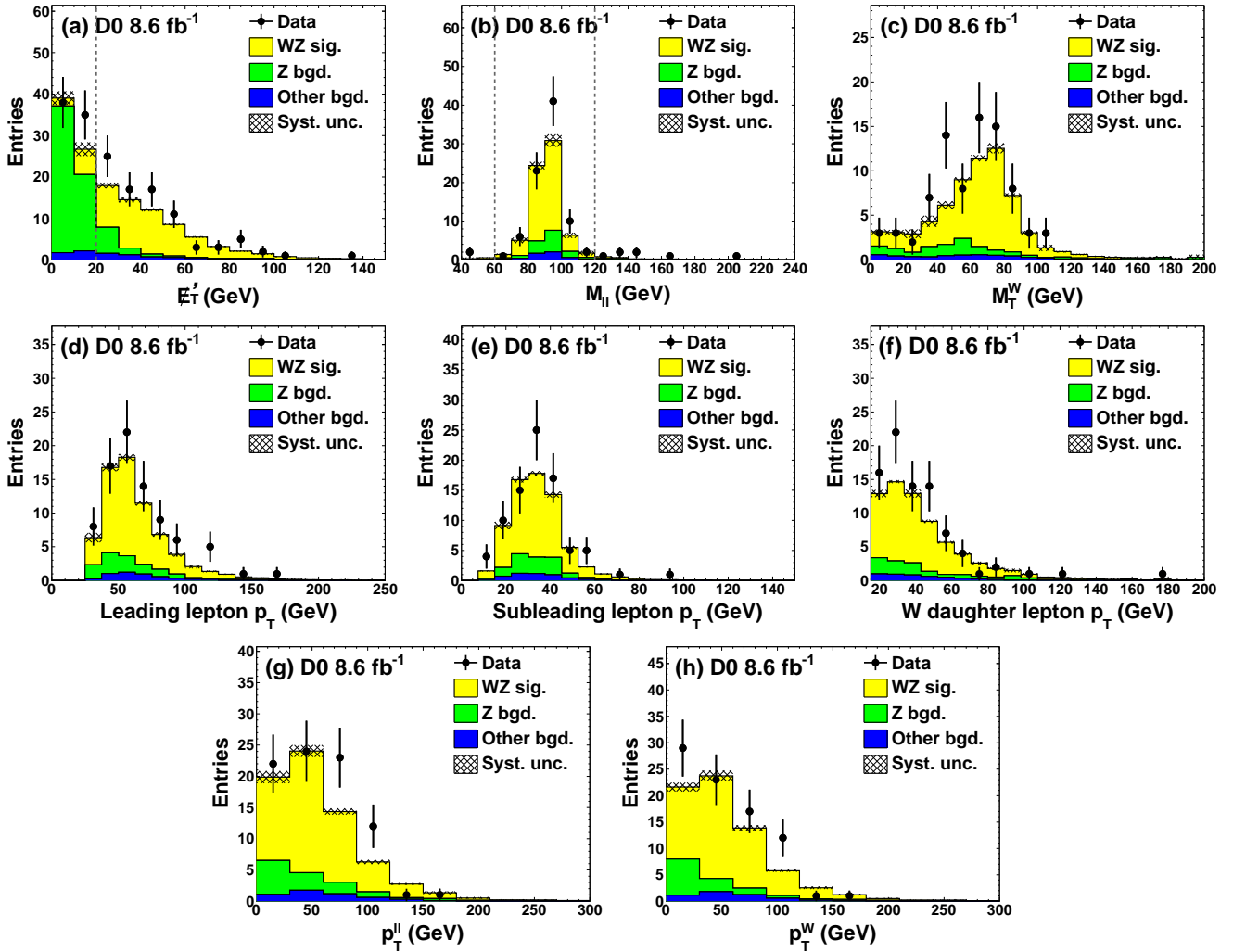 (h) $W \to l\nu$ decays. The vertical dashed lines indicate the requirements on $\not{E}_T'$ and $M_{\ell\ell}$. The signal normalization is as described in Section IV.
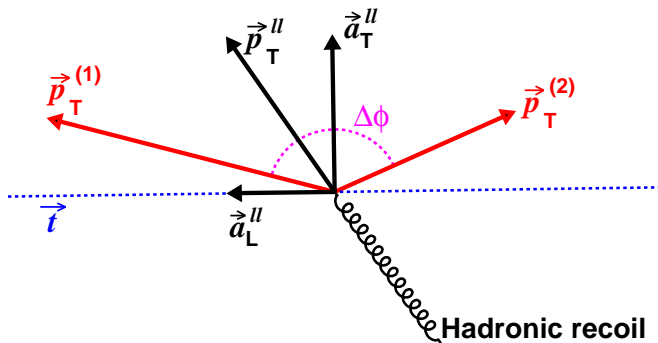
FIG. 4: Illustration of the decomposition of the dilepton p_T into a_T and a_L components.

that are reconstructed close to module boundaries in the CC or in the IC have relatively poor energy resolution and are given special treatment. The estimated uncertainty may be inflated to cover the difference between the calorimeter based p_T measurement and the alternative measurement from the central track. This is only allowed for the upward variation and protects against electrons for which the calorimeter has severely undermeasured the energy. The amount by which, e.g., $a_T^{\ell\ell}$ is reduced, is denoted a_T^{δ}. These quantities are defined in such a way that they always carry a negative sign.

B. Calorimeter recoil

Two estimates of the calorimeter recoil are made, from the reconstructed jets and from the reconstructed $\not{E}_T$.
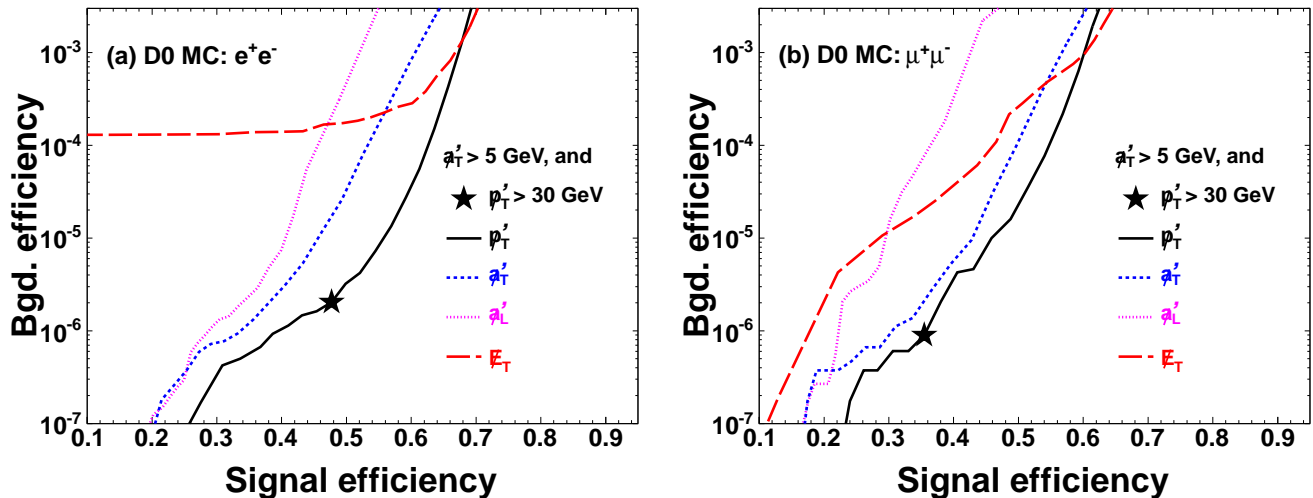
FIG. 5: Background vs. signal efficiency for (a) e^+e^- and (b) $\mu^+\mu^-$ channels after varying the requirements on variables that are sensitive to the missing transverse momentum. The requirement $\not{d}'_T > 5$ GeV is always applied.

Jets are reconstructed using the D0 mid-point cone algorithm [29] with a cone size of $\Delta\mathcal{R} = 0.5$. They must be separated from the leptons by at least $\Delta\mathcal{R} > 0.3$ and satisfy $p_T > 15$ GeV. The p_T, a_T, and a_L components are calculated for each jet in the event, e.g.,

$$a_T^{\text{jet(i)}} = \vec{p}_T^{\,\text{jet(i)}} \times \hat{t}, \qquad (8)$$

where $\vec{p}_T^{\,\text{jet(i)}}$ is the p_T vector of the ith jet. An individual jet that has a positive value (i.e., *increases* the momentum imbalance) is ignored. This approach ensures that jets which are not genuinely associated with the recoil system (e.g., from additional $p\bar{p}$ collisions or the underlying event) are not allowed to generate a fake imbalance in an otherwise well reconstructed event. The sum of contributions from the jets is denoted, e.g., for the a_T component, a_T^{jets}.

The $\not{E}_T$ estimate subtracts any contribution from the two leptons and then tests how well the remaining $\not{E}_T$ balances the dilepton system. Between the jet and $\not{E}_T$ based corrections we choose (separately for the a_T, a_L and p_T components) the one that best balances the dilepton system. This correction term is denoted, e.g., a_T^{recoil}.

C. Track recoil

As a protection against events in which at least one hadronic jet fails to be reconstructed in the calorimeter, we attempt to recover any remaining activity in the tracker. Track jets are reconstructed by merging together reconstructed tracks within cones of size $\Delta\mathcal{R} = 0.5$. These tracks must satisfy $p_T > 1$ GeV. Track jets must have at least two tracks within the cone, and be separated by at least $\Delta\mathcal{R} = 0.3$ from the leptons, and by at least $\Delta\mathcal{R} = 0.5$ from any calorimeter jets. Corrections to

each of the (p_T, a_T, and a_L) components are determined in the same way as for calorimeter jets.

D. Performance

Figure 5 shows the $Z \to \ell^+\ell^-$ background efficiency versus the $ZZ \to \ell^+\ell^-\nu\bar{\nu}$ signal efficiency for a range of requirements on each of the variables; $\not{d}'_T$, $\not{d}'_L$, $\not{p}'_T$, and $\not{E}_T$. The decays of $Z \to \tau^+\tau^-$ into e^+e^-, $\mu^+\mu^-$, and $e^\pm\mu^\mp$ final states produce a genuine missing p_T along the a_L direction. Our $ZZ \to \ell^+\ell^-\nu\bar{\nu}$ candidate selection requirements therefore include a "soft" requirement of $\not{d}'_T > 5$ GeV. The curves in Fig. 5 correspond to the combination of this requirement and a varying requirement on the variable under study. The $\not{p}'_T$ variable has the best performance over the range of background efficiencies of interest. The efficiency for the requirement $\not{p}'_T > 30$ GeV (and $\not{d}'_T > 5$ GeV) is indicated explicitly by a star symbol. This is the requirement that is made in selecting $ZZ \to \ell^+\ell^-\nu\bar{\nu}$ candidates. The optimisation of the $\not{p}'_T$ requirement is discussed later.

VII. SELECTION OF ZZ CANDIDATES

Decays of ZZ into the following final states are considered: $e^+e^-\nu\bar{\nu}$, $\mu^+\mu^-\nu\bar{\nu}$. Events must contain two oppositely charged tight quality leptons satisfying the p_T requirements described earlier and with $M_{\ell\ell}$ between 60 and 120 GeV. To reject events in which the missing transverse momentum estimators defined in Section VI are poorly reconstructed, we require that there are no more than two jets with $p_T > 15$ GeV and separated by at least $\Delta\mathcal{R} = 0.3$ from the leptons. In order to reject $WZ \to \ell^\pm\nu\ell^+\ell^-$ and $ZZ \to \ell^+\ell^-\ell^+\ell^-$ events, there

must be no additional EM clusters or muons according to the criteria in Section V. In addition, there must be no isolated tracks or hadronic taus with $p_T > 5$ GeV. This requirement is not necessary in the WZ analysis, for which the $ZZ \to \ell^+\ell^-\ell^+\ell^-$ background is less significant. These four types of objects are only considered if they are separated by at least $\Delta\mathcal{R} = 0.3$ from the leptons. The jet and additional lepton vetoes are also effective in suppressing the background from $t\bar{t} \to \ell^+\ell^-\nu\bar{\nu}b\bar{b}$ decays. The number of events that satisfy these requirements is used as the denominator in the measurement of the ZZ/Z cross section ratio. Including the jet and lepton vetoes in the Z selection helps to reduce the impact of uncertainties in the corresponding efficiencies.

Events are considered as $ZZ \to \ell^+\ell^-\nu\bar{\nu}$ candidates if they further satisfy $\not{p}'_T > 5$ GeV (to reject $Z \to \tau^+\tau^-$) and $\not{p}'_T > 30$ GeV (to reject $Z \to e^+e^-$ and $Z \to \mu^+\mu^-$). Tables III, IV and V show, for the three sub-channels, the predicted yields for each process. The yields are also presented for events that fail each requirement exclusively. Figure 6 shows the $\not{p}'_T$ and $M_{\ell\ell}$ distributions before imposing their respective requirements. A neural network (NN) is trained to discriminate $ZZ \to \ell^+\ell^-\nu\bar{\nu}$ from the dominant background in the final event sample ($WW \to \ell^+\nu\ell^-\bar{\nu}$). The following input variables are used: the p_T of each lepton, the $\not{E}_T$, the center of mass scattering angle $\cos\theta^*_\eta$ [30], the azimuthal angle between the leading lepton and the dilepton system $\Delta\phi(\ell_1,\ell\ell)$, and $(M_{\ell\ell} - m_Z)/\sigma(M_{\ell\ell})$ where $\sigma(M_{\ell\ell})$ is the estimated uncertainty on the measured dilepton invariant mass. Figure 6 also shows the NN output distribution of the selected signal candidate events. Separate NNs are trained for the e^+e^- and $\mu^+\mu^-$ channels, and the e^+e^- version is shown for the $e^\pm\mu^\mp$ channel. Figure 7 shows a number of kinematic distributions for the combination of $ZZ \to e^+e^-\nu\bar{\nu}$ and $ZZ \to \mu^+\mu^-\nu\bar{\nu}$ candidate events.

Figure 8 shows how the predicted ZZ cross section measurement uncertainty varies as a function of the $\not{p}'_T$ requirement. The expected systematic uncertainty rises rapidly below 25 GeV as the $Z \to \ell^+\ell^-$ background starts to contaminate the sample. The requirement $\not{p}'_T > 30$ GeV is close to the minimum and is in a region where the systematic uncertainty is small.

VIII.   SYSTEMATIC UNCERTAINTIES

We measure the ratios of WZ and ZZ cross sections relative to the inclusive Z boson cross section. Lepton reconstruction, identification, and trigger efficiency uncertainties are largely cancelled in the ratio, as are those arising from the vetoes on additional lepton candidates or other activity. The WZ analysis is sensitive to the lepton identification efficiencies, since the signal and $Z \to \ell^+\ell^-$ samples differ by the requirement of an additional tight quality reconstructed electron or muon. The ZZ analysis is sensitive to the modeling of the diboson p_T, since requirements on the missing p_T estimators are less efficient in signal events with a large hadronic recoil. Tables VI and VII list the sources of systematic uncertainty on the WZ and ZZ cross section measurements, respectively. We list the fractional variations in the number of predicted background events N_{bgd}, the acceptances (multiplied by efficiencies) for signal (A_{sig}) and $Z \to \ell^+\ell^-$ ($A_{\ell\ell}$), and the measured signal cross section σ_{sig}. The following sources of systematic uncertainty are considered.

- **Beam conditions**
  The differential distributions of the instantaneous luminosity and vertex z position are varied to cover any disagreement with the data.

- **Physics modeling**
  The value of the g_2 parameter in RESBOS is varied when determining the corrections that are applied to the simulated $Z \to \ell^+\ell^-$ events. This is a model parameter that describes the intrinsic transverse momentum of the partons within the colliding hadrons. As a test of sensitivity to the diboson p_T modeling, the reweighting in this variable is switched off.

- **Jet reconstruction**
  The jet energy scale, resolution, and reconstruction efficiencies are varied within their uncertainties. The simulation requires additional corrections to the energy response for jets in the IC region. An additional systematic uncertainty is assigned to these corrections. The track jet reconstruction efficiency is also varied to cover an observed disagreement with the data.

- **Lepton momentum scale and resolution**
  The lepton momentum scales and resolutions are varied within their uncertainties, as are the reconstruction and identification efficiencies. Non-Gaussian tails in the lepton momentum resolution are also considered.

- **Instrumental backgrounds**
  The W+jets and Z+jets background normalizations are varied within the uncertainties of the estimate from data. All other variations on the simulation (e.g., lepton momentum scales and resolutions) are allowed to vary the shape of these backgrounds. Since PYTHIA does not include the matrix element for wide angle photon emission in $W\gamma$ production, the normalization of this process is varied by a factor of two, which is considered to be an overestimate but introduces no significant uncertainty on the ZZ cross section measurement.

- **Trigger efficiencies**
  The trigger efficiencies are estimated to introduce a negligible uncertainty into the cross section measurements.
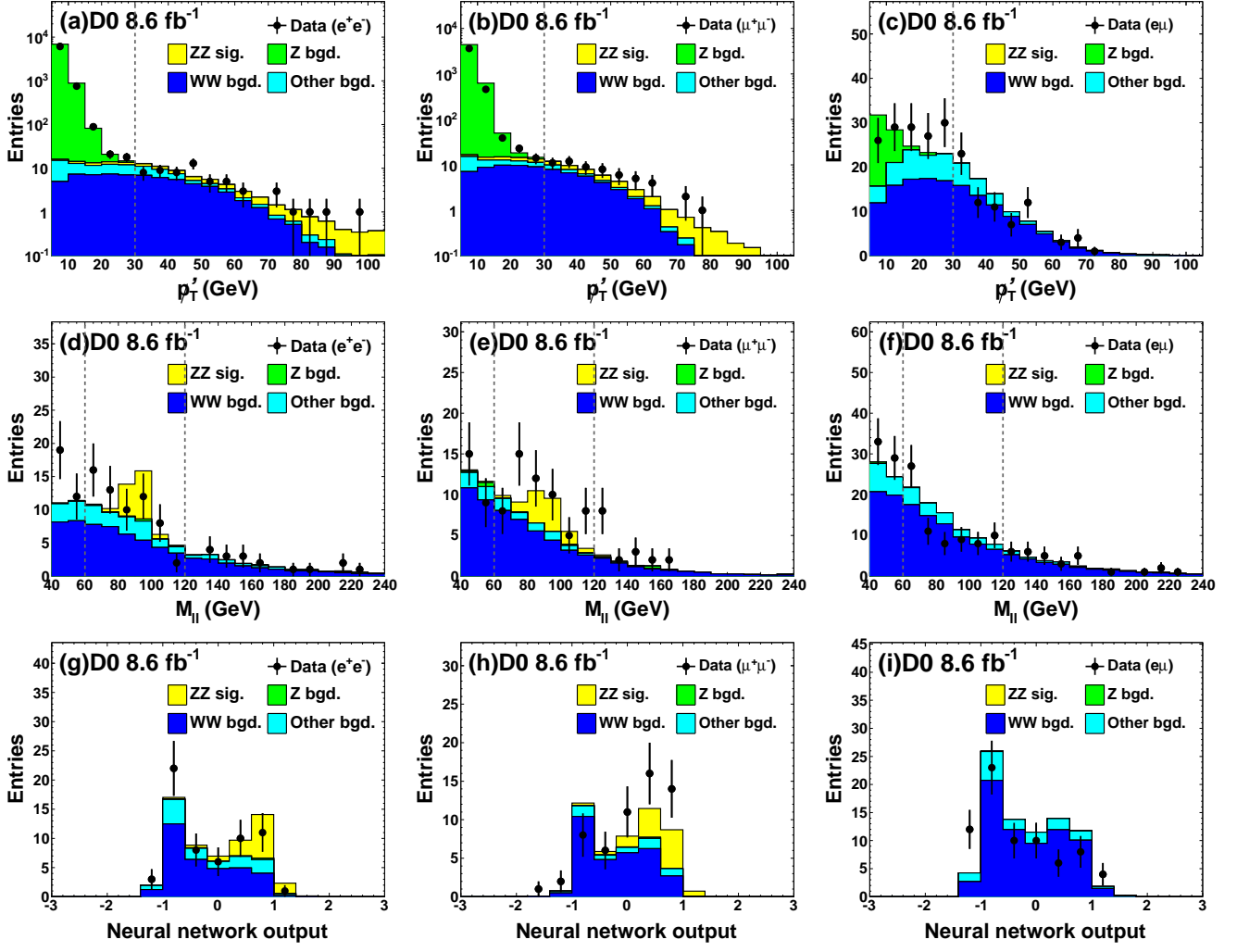
FIG. 6: (a-c) The $\not{p}'_T$ distribution of the $ZZ \to \ell^+\ell^-\nu\bar{\nu}$ candidate events before imposing the $\not{p}'_T$ requirement. (d-f) The $M_{\ell\ell}$ distribution of the $ZZ \to \ell^+\ell^-\nu\bar{\nu}$ candidate events before imposing the $M_{\ell\ell}$ requirement. (g-i) The neural network output distribution of the accepted $ZZ \to \ell^+\ell^-\nu\bar{\nu}$ candidate events. For the $e^\pm\mu^\mp$ channel, the neural network trained in the e^+e^- channel is shown. The vertical dashed lines indicate the requirements on $\not{p}'_T$ and $M_{\ell\ell}$. The signal normalization is as described in Section IV.

TABLE III: Table of predicted signal and background yields for the $ZZ \to e^+e^-\nu\bar{\nu}$ signal and control regions. The systematic uncertainties are provided for the predictions.

| | | | | Rejected by requirement on | | | |
Process	Accepted	$\not{p}'_T$	$\not{\phi}'_T$	M_{ll}	Extra lep.	Charge	Jets
$Z \to e^+e^-$	0.6 ± 0.3	11666 ± 1665	0 ± 1	0.3 ± 0.2	3 ± 2	–	0.1 ± 0.1
$Z \to \tau^+\tau^-$	0.1 ± 0.1	8 ± 2	1.4 ± 0.2	–	–	–	–
$WW \to \ell^+\nu\ell^-\bar{\nu}$	35 ± 1	35 ± 1	1.7 ± 0.1	33 ± 1	9 ± 5	0.3 ± 0.1	0.1 ± 0.1
$WZ \to \ell^\pm\nu\ell^+\ell^-$	2.3 ± 0.1	1.9 ± 0.1	0.2 ± 0.0	0.2 ± 0.1	14 ± 2	0.2 ± 0.1	–
$W \to e\nu$	6 ± 2	13 ± 2	0.3 ± 0.1	5 ± 1	2 ± 1	4 ± 1	–
$W\gamma \to e\nu\gamma$	3.3 ± 0.3	5.5 ± 0.5	0.0 ± 0.1	2.8 ± 0.5	0.6 ± 0.5	3.3 ± 0.4	–
$ZZ \to \ell^+\ell^-\ell^+\ell^-$	–	0.1 ± 0.0	–	–	1.3 ± 0.2	–	–
$t\bar{t} \to \ell^+\ell^-\nu\bar{\nu}b\bar{b}$	1.0 ± 0.2	1.4 ± 0.2	0.4 ± 0.1	1.2 ± 0.1	7 ± 1	–	0.2 ± 0.1
Predicted background	48 ± 2	11749 ± 1668	4 ± 1	43 ± 2	37 ± 11	8 ± 1	0.4 ± 0.2
$ZZ \to \ell^+\ell^-\nu\bar{\nu}$	13.6 ± 0.4	7.4 ± 0.2	1.3 ± 0.1	0.6 ± 0.0	4 ± 2	0.2 ± 0.0	0.1 ± 0.0
Predicted total	62 ± 3	11756 ± 1668	6 ± 1	43 ± 2	41 ± 13	8 ± 1	0.4 ± 0.2
Observed	61	10560	12	50	63	12	1
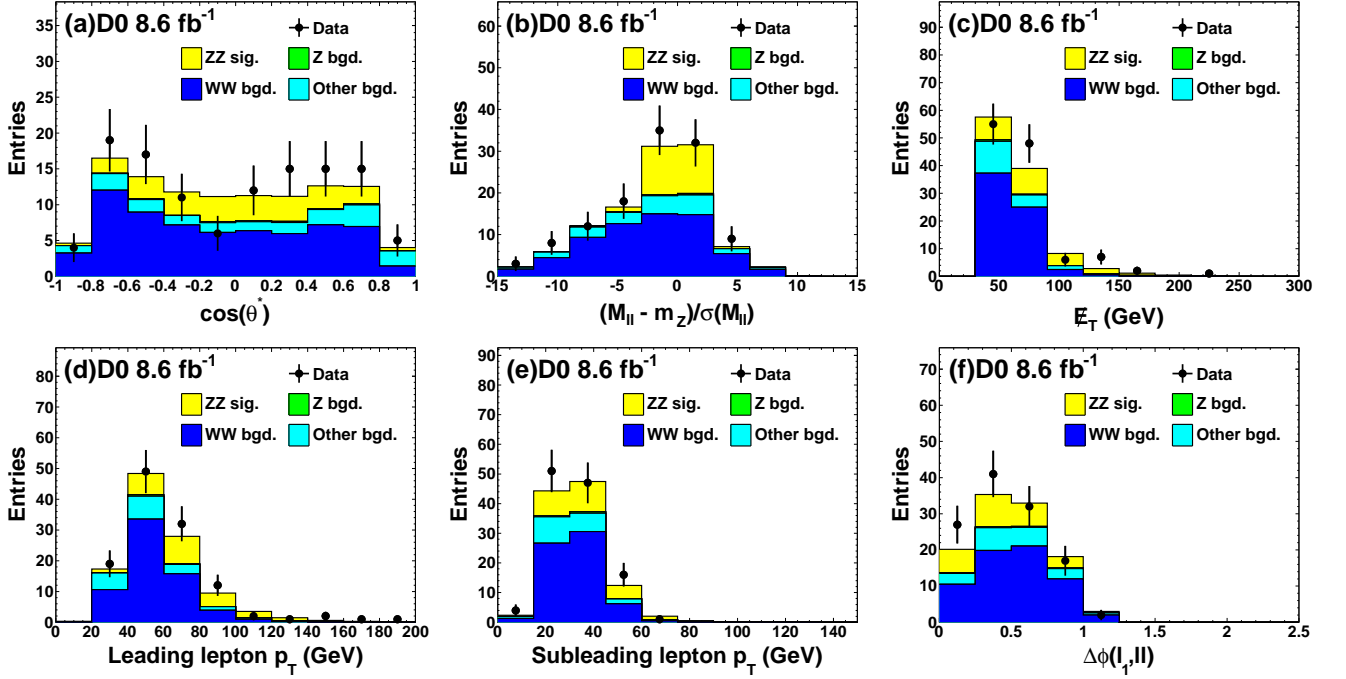
FIG. 7: Distributions of (a) $\cos(\theta^*)$, (b) $(M_{\ell\ell} - m_Z)/\sigma(M_{\ell\ell})$, (c) $\not{E}_T$, transverse momenta of the (d) leading and (e) sub-leading lepton, (f) the azimuthal angle between the leading lepton and the dilepton system $\Delta\phi(\ell_1, \ell\ell)$ for the combination of $ZZ \to e^+e^-\nu\bar{\nu}$ and $ZZ \to \mu^+\mu^-\nu\bar{\nu}$ candidates. The signal normalization is as described in Section IV.
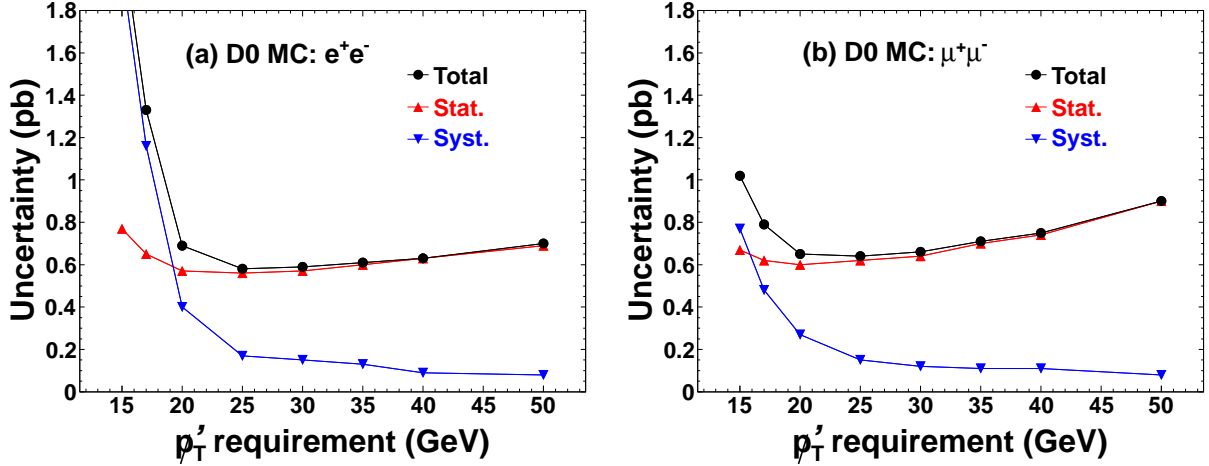

FIG. 8: Variation of the predicted uncertainties on the measured ZZ cross section with the choice of $\not{p}_T'$ requirement in the (a) e^+e^- and (b) $\mu^+\mu^-$ channels.

IX. MEASUREMENT OF CROSS SECTIONS

The ratios of the signal (WZ or ZZ) cross sections to the inclusive Z boson cross section are determined as follows:

$$\mathcal{R} = \frac{N_{\mathrm{sig}}^{\mathrm{obs}}/(A_{\mathrm{sig}} \times B_{\mathrm{sig}} \times \mathcal{L})}{N_{\ell\ell}^{\mathrm{obs}}/(A_{\ell\ell} \times B_{\ell\ell} \times \mathcal{L})},$$

where $\mathcal{L}$ is the integrated luminosity; $B_{\ell\ell}$ and B_{sig} are the known branching fractions for $Z \to \ell^+\ell^-$ and the signal

decay, respectively [27]. We choose an acceptance window of $60 < M_{\ell\ell} < 120$ GeV.

The number of observed signal events, $N_{\mathrm{sig}}^{\mathrm{obs}}$ is determined by allowing the predicted signal yield to float such that the following likelihood function is maximized:

$$L = \prod_{i=0}^{\mathrm{bins}} \mathcal{P}(N_i^{\mathrm{obs}}; N_i^{\mathrm{pred}}), \qquad (9)$$

where $\mathcal{P}$ is the Poisson probability to observe N_i^{obs} events

TABLE IV: Table of predicted signal and background yields for the $ZZ \to \mu^+\mu^-\nu\bar\nu$ signal and control regions. The systematic uncertainties are provided for the predictions.

Process	Accepted	$p\!\!\!/_T'$	$\phi\!\!\!/_T'$	M_{ll}	Extra lep.	Charge	Jets
$Z \to \mu^+\mu^-$	0.3 ± 0.5	8519 ± 1372	3 ± 6	2 ± 2	3 ± 2	0.4 ± 0.1	0.1 ± 0.1
$Z \to \tau^+\tau^-$	–	5 ± 3	1.4 ± 0.3	–	0.1 ± 0.0	–	–
$WW \to \ell^+\nu\ell^-\bar\nu$	31 ± 2	48 ± 2	1.4 ± 0.2	29 ± 2	9 ± 5	–	0.1 ± 0.1
$WZ \to \ell^\pm\nu\ell^+\ell^-$	2.0 ± 0.1	2.9 ± 0.2	0.2 ± 0.0	0.3 ± 0.0	12 ± 2	0.2 ± 0.1	–
$W \to \mu\nu$	2.3 ± 0.4	9 ± 2	0.0 ± 0.1	2.9 ± 0.7	1.1 ± 0.9	0.8 ± 0.2	–
$ZZ \to \ell^+\ell^-\ell^+\ell^-$	–	0.2 ± 0.0	–	–	0.9 ± 0.2	–	–
$t\bar t \to \ell^+\ell^-\nu\bar\nu b\bar b$	0.8 ± 0.1	2.0 ± 0.2	0.4 ± 0.1	0.9 ± 0.1	6 ± 1	–	0.2 ± 0.1
Predicted background	36 ± 2	8602 ± 1374	6 ± 6	36 ± 2	32 ± 9	1.4 ± 0.2	0.4 ± 0.3
$ZZ \to \ell^+\ell^-\nu\bar\nu$	11.8 ± 0.3	11.0 ± 0.3	0.9 ± 0.1	0.8 ± 0.1	4 ± 2	–	–
Predicted total	48 ± 2	8613 ± 1374	7 ± 6	36 ± 2	35 ± 11	1.4 ± 0.2	0.4 ± 0.3
Observed	58	7416	7	42	60	4	1

TABLE V: Table of predicted yields in the $e^\pm\mu^\mp$ channel. The systematic uncertainties are provided for the predictions.

Process	Accepted	$p\!\!\!/_T'$	$\phi\!\!\!/_T'$	M_{ll}	Extra lep.	Charge	Jets
$Z \to e^+e^-$	–	17 ± 7	–	–	–	–	–
$Z \to \mu^+\mu^-$	–	6 ± 2	–	0.3 ± 0.3	0.3 ± 0.1	–	–
$Z \to \tau^+\tau^-$	0.1 ± 0.1	19 ± 14	4.5 ± 0.4	0.1 ± 0.1	0.2 ± 0.2	–	–
$WW \to \ell^+\nu\ell^-\bar\nu$	69 ± 3	84 ± 4	3.7 ± 0.2	67 ± 3	19 ± 11	0.4 ± 0.1	0.3 ± 0.2
$WZ \to \ell^\pm\nu\ell^+\ell^-$	0.4 ± 0.1	0.7 ± 0.1	–	0.4 ± 0.1	3.3 ± 0.6	0.4 ± 0.1	–
$W \to e\nu$	4 ± 2	9 ± 3	0.1 ± 0.2	5 ± 1	1 ± 1	1.2 ± 0.6	–
$W \to \mu\nu$	5 ± 4	12 ± 9	0.2 ± 0.1	5 ± 4	1 ± 2	3 ± 2	–
$W\gamma \to e\nu\gamma$	3.4 ± 0.5	6.4 ± 0.4	0.1 ± 0.1	3.4 ± 0.3	0.7 ± 0.6	3.2 ± 0.3	–
$ZZ \to \ell^+\ell^-\ell^+\ell^-$	–	–	–	–	0.2 ± 0.0	–	–
$t\bar t \to \ell^+\ell^-\nu\bar\nu b\bar b$	2.3 ± 0.2	3.3 ± 0.2	1.0 ± 0.1	2.1 ± 0.2	13 ± 3	–	0.3 ± 0.1
Predicted background	84 ± 6	157 ± 19	9.6 ± 0.5	83 ± 6	39 ± 16	8 ± 3	0.5 ± 0.3
$ZZ \to \ell^+\ell^-\nu\bar\nu$	–	–	–	0.1 ± 0.0	–	–	–
Predicted total	84 ± 6	157 ± 19	9.6 ± 0.5	83 ± 6	39 ± 16	8 ± 3	0.5 ± 0.3
Observed	73	162	7	96	60	8	0

in the ith bin, given a prediction of N_i^{pred}. In the WZ analysis, the M_T distribution is used, while the neural network output distribution is used in the ZZ analysis. The 68% C.L. interval on the signal yield is defined by $\delta(\ln L) = 0.5$, with respect to the maximum of $\ln L$.

Table VIII lists, for the six different sub-channels, the ratios of inclusive Z and signal acceptances that are estimated from the simulation. Table IX lists the measured $\mathcal{R}$ values. The p-values for consistency of the different sub-channels are 54% and 11% for the WZ and ZZ analyses, respectively, evaluated using a χ^2 test. For the combination of respective sub-channels, we measure:

$$\mathcal{R}(WZ) = 0.593 \pm 0.080(\mathrm{stat}) \pm 0.017(\mathrm{syst})(\times 10^{-3}),$$

$$\mathcal{R}(ZZ) = 0.216 \pm 0.058(\mathrm{stat}) \pm 0.017(\mathrm{syst})(\times 10^{-3}).$$

A theoretical calculation of the Z cross section can be used to translate these into signal cross section measurements. The product of the cross section and branching fraction for $Z \to \ell^+\ell^-$ (one lepton flavor) is calculated using a modified version of the next-to-NLO (NNLO) code of Ref. [31] with the MRST2004 NNLO PDFs [32]. Since this code excludes the γ^* and Z/γ^* interference, a correction factor is determined using PYTHIA and the NLO event generator MC@NLO [33]. For $60 < M_{\ell\ell} < 120$ GeV, the result is,

$$\sigma(p\bar p \to Z/\gamma^*) \times B_{\ell\ell} = 255.8\ {}^{+5.1}_{-12.0}\ \mathrm{pb},$$

where the uncertainties arise from variations in the PDFs and the renormalization and factorization scales, and with $B_{\ell\ell} = 3.3658 \pm 0.0023$ % [27]. The measured WZ cross section with $60 < M_{\ell\ell} < 120$ GeV is

$$\sigma(p\bar p \to WZ) = 4.50 \pm 0.61(\mathrm{stat})^{+0.16}_{-0.25}(\mathrm{syst})\ \mathrm{pb}.$$

This result is slightly larger than, but still consistent with a prediction of 3.21 ± 0.19 pb from the NLO program MCFM [34] with the MSTW2008 NLO PDFs [35], and

TABLE VI: Table of uncertainty sources in the WZ cross section measurement after combining the four sub-channels. All values are given in percent.

	N_{bgd}	$A_{\ell\ell}$	A_{sig}	$A_{\ell\ell}/A_{\mathrm{sig}}$	σ_{sig}
L_{inst} profile	4.0	2.4	3.3	0.9	0.2
Vertex z profile	1.6	1.3	0.9	0.4	0.7
$Z/\gamma^* p_T$	0.0	0.0	0.0	0.0	0.2
Diboson p_T	0.1	0.0	0.4	0.4	0.2
Jet energy scale	6.0	0.1	0.3	0.2	1.3
Jet energy resol.	2.2	0.0	0.0	0.0	0.2
IC jet treatment	1.1	0.0	0.0	0.0	0.2
Electron p_T scale	0.3	0.0	0.1	0.1	0.2
Electron p_T resol.	1.0	0.1	0.0	0.0	0.2
Electron p_T tails	0.1	0.0	0.3	0.4	0.2
Muon p_T scale	0.1	0.0	0.1	0.1	0.2
Muon p_T resol.	0.9	0.1	0.1	0.0	0.2
Muon p_T tails	1.0	0.2	0.4	0.2	0.2
Track reconstr.	0.1	0.7	1.1	0.3	0.7
Muon reconstr.	0.2	0.3	0.5	0.2	0.2
Electron reconstr.	0.2	0.2	0.2	0.0	0.2
Z/γ^*+jets model.	17.7	0.0	0.0	0.0	2.5
Systematic	19.4	2.9	3.7	1.2	3.1
Statistical	–	–	–	–	13.2
Stat. $\oplus$ syst.	19.4	2.9	3.7	1.2	13.6

TABLE VII: Table of uncertainty sources in the ZZ cross section measurement after combining the e^+e^- and $\mu^+\mu^-$ channels. All values are given in percent.

	N_{bgd}	$A_{\ell\ell}$	A_{sig}	$A_{\ell\ell}/A_{\mathrm{sig}}$	σ_{sig}
L_{inst} profile	1.5	4.5	5.2	0.7	1.8
Vertex z profile	1.0	1.3	0.7	0.6	2.5
$Z/\gamma^* p_T$	0.0	0.0	0.0	0.0	0.6
Diboson p_T	2.6	0.0	1.8	1.8	3.7
Jet energy scale	1.1	0.8	1.5	0.8	1.8
Jet energy resol.	0.9	0.1	0.1	0.0	1.8
IC jet treatment	0.2	0.2	0.4	0.2	0.6
Jet reconstr.	0.5	0.3	0.0	0.2	0.0
Trkjet reconst.	1.5	0.0	1.1	1.2	3.1
Electron p_T scale	0.4	0.0	0.0	0.0	0.6
Electron p_T resol.	1.0	0.1	0.5	0.4	1.8
Electron p_T tails	1.0	0.0	0.6	0.6	1.2
Muon p_T scale	0.1	0.0	0.0	0.0	0.0
Muon p_T resol.	0.5	0.1	0.5	0.5	0.6
Muon p_T tails	0.1	0.1	0.5	0.4	0.6
Lepton eff. vs p_T	0.0	0.0	0.0	0.0	0.6
Lepton eff. vs η	0.0	0.0	0.0	0.0	0.6
W+jets model.	1.9	0.0	0.0	0.0	0.6
$W\gamma$ model.	3.9	0.0	0.0	0.0	1.8
Systematic	6.0	4.8	6.0	2.6	7.1
Statistical	–	–	–	–	27.0
Stat. $\oplus$ syst.	6.0	4.8	6.0	2.6	27.9

Sub-channel	$A_{\ell\ell}/A_{\mathrm{sig}}$	$N_{\ell\ell}^{\mathrm{obs}}$
$WZ \to e^\pm \nu e^+ e^-$	2.242 ± 0.025	459336
$WZ \to \mu^\pm \nu e^+ e^-$	1.495 ± 0.023	419069
$WZ \to e^\pm \nu \mu^+ \mu^-$	1.704 ± 0.027	493202
$WZ \to \mu^\pm \nu \mu^+ \mu^-$	1.443 ± 0.023	443869
$ZZ \to e^+ e^- \nu\bar\nu$	1.638 ± 0.049	319797
$ZZ \to \mu^+ \mu^- \nu\bar\nu$	2.052 ± 0.059	342603

TABLE VIII: Table of acceptance ratios for the different sub-channels, where the quoted uncertainties are systematic. Also shown are the numbers of observed events at the dilepton selection stage, $N_{\ell\ell}^{\mathrm{obs}}$.

setting the renormalization and factorization scales equal to $m_W + m_Z$. The measured ZZ cross section with $60 < M_{\ell\ell} < 120$ GeV is

$$\sigma(p\bar{p} \to ZZ) = 1.64 \pm 0.44(\mathrm{stat})^{+0.13}_{-0.15}(\mathrm{syst}) \text{ pb.}$$

This can be compared to a prediction of 1.30 ± 0.10 pb from MCFM setting the renormalization and factorization scales equal to $2m_Z$. For comparing to and combining with previous measurements it is more convenient to correct the cross sections for the presence of diagrams involving γ^*. A correction of $+3.4\%$ is obtained by comparing ZZ cross sections with and without γ^* and Z/γ^* interference from MCFM [34]. Combining this corrected ZZ cross section with a previous D0 measurement [9] in the $ZZ \to \ell^+\ell^-\ell^+\ell^-$ channel yields

$$\sigma(p\bar{p} \to ZZ) = 1.44^{+0.31}_{-0.28}\,(\mathrm{stat})\,^{+0.17}_{-0.19}\,(\mathrm{syst}) \text{ pb.}$$

X. CONCLUSIONS

We measure the production cross sections for the processes $p\bar{p} \to WZ \to \ell^\pm\nu\ell^+\ell^-$ and $p\bar{p} \to ZZ \to \ell^+\ell^-\nu\bar\nu$, using 8.6 fb^{-1} of integrated luminosity collected by the D0 experiment at the Fermilab Tevatron collider. For decay channels involving electrons and muons, we observe agreement between the different sub-channels as can be seen in Fig. 9. Combining the sub-channels yields a WZ cross section of $4.50^{+0.63}_{-0.66}$ pb, which is slightly larger

than, but still consistent with the standard model prediction of 3.21 ± 0.19 pb. The ZZ cross section is measured to be 1.64 ± 0.46 pb, which is also in agreement with a standard model prediction of 1.30 ± 0.10 pb. These are the most precise measurements to date of the WZ and ZZ cross sections in $p\bar{p}$ collisions at $\sqrt{s} = 1.96$ TeV. Correcting for the contribution from γ^* and Z/γ^* interference and combining with a previous measurement in the $\ell^+\ell^-\ell^+\ell^-$ channel yields a ZZ cross section of $1.44^{+0.35}_{-0.34}$ pb.

Sub-channel	$\mathcal{R}(\times 10^{-3})$
$WZ \to e^{\pm}\nu e^{+}e^{-}$	0.70 ± 0.20
$WZ \to \mu^{\pm}\nu e^{+}e^{-}$	0.40 ± 0.14
$WZ \to e^{\pm}\nu \mu^{+}\mu^{-}$	0.66 ± 0.17
$WZ \to \mu^{\pm}\nu \mu^{+}\mu^{-}$	0.61 ± 0.16
$ZZ \to e^{+}e^{-}\nu\bar{\nu}$	0.13 ± 0.07
$ZZ \to \mu^{+}\mu^{-}\nu\bar{\nu}$	0.33 ± 0.10

TABLE IX: Table of $\mathcal{R}$ values measured for each of the sub-channels, where the uncertainties correspond to statistical and systematic components added in quadrature.

[1] K. Hagiwara, S. Ishihara, R. Szalapski, and D. Zeppenfeld, Phys. Rev. D **48**, 2182 (1993).
[2] U. Baur and D. Rainwater, Phys. Rev. D **62**, 113011 (2000).
[3] A. Abulencia *et al.*, Phys. Rev. Lett. **98**, 161801 (2007).
[4] D0 Collaboration, V. Abazov *et al.*, Phys. Rev. D **64**, 111104 (2007).
[5] V. Abazov *et al.*, Phys. Lett. B **695**, 67 (2011).
[6] V. Abazov *et al.*, Phys. Rev. Lett. **101**, 171803 (2008).
[7] V. Abazov *et al.*, Phys. Rev. D **78**, 072002 (2008).
[8] T. Aaltonen *et al.*, Phys. Rev. Lett. **100**, 201801 (2008).
[9] V. Abazov *et al.*, Phys. Rev. D **84**, 011103 (2011).
[10] This cross section is corrected for the γ^{*} contribution.
[11] CDF Collaboration, T. Aaltonen *et al.*, arXiv:1112.2978 [hep-ex] (2011).
[12] ATLAS Collaboration, G. Aad *et al.*, arXiv:1111.5570 [hep-ex] (2011).
[13] ATLAS Collaboration, G. Aad *et al.*, arXiv:1110.5016 [hep-ex] (2011).
[14] V. Abazov *et al.*, Nucl. Instrum. Methods Phys. Res. A **565**, 463 (2006).
[15] M. Abolins *et al.*, Nucl. Instrum. Methods Phys. Res. A **584**, 75 (2008).
[16] S. Ahmed *et al.*, Nucl. Instrum. Methods Phys. Res. A **634**, 8 (2011).
[17] Rapidity is defined by $y = (1/2)\ln[(E - p_z)/(E + p_z)]$, where E is the energy and p_z is the momentum component parallel to the proton beam direction. Pseudorapidity is defined by $\eta = -\ln[\tan(\theta/2)]$, where θ is the polar angle measured relative to the center of the detector.
[18] A. Hoecker *et al.*, CERN-OPEN 007 (2007).
[19] We define $(\Delta\mathcal{R})^2 = (\Delta\phi)^2 + (\Delta\eta)^2$, where $\Delta\phi$ and $\Delta\eta$ are the differences between two objects in azimuth and pseudorapidity, respectively.
[20] T. Sjostrand *et al.*, Comput. Phys. Commun. **135**, 238 (2001).
[21] D. Stump *et al.*, J. High Energy Phys. **10**, 046 (2003).
[22] R. Brun and F. Carminati, CERN Program Library Long Writeup W5013, 1993.
[23] C. Balazs and C.-P. Yuan, Phys. Rev. D **56**, 5558 (1997).
[24] P. Nason, J. High Energy Phys. **11**, 40 (2004).
[25] S. Frixione, P. Nason, and C. Oleari, J. High Energy Phys. **11**, 70 (2007).
[26] D0 Collaboration, V. Abazov *et al.*, Phys. Rev. D **76**, 092007 (2007).
[27] K. Nakamura *et al.*, J. Phys. G **37**, 075021 (2010).
[28] M. Vesterinen and T. Wyatt, Nucl. Instrum. Methods Phys. Res. A **602**, 432 (2009).
[29] G. Blazey *et al.*, in *Proceedings of the Workshop: QCD and Weak Boson Physics in Run II*, edited by U. Baur, R. Ellis, and D. Zeppenfeld, 2000, Fermilab-Pub-00/297.
[30] A. Banfi, S. Redford, M. Vesterinen, P. Waller, and T. R. Wyatt, Eur. Phys. J. C **71**, 2011 (1600).
[31] R. Hamberg, W. van Neerven, and T. Matsuura, Nucl. Phys. B **359**, 343 (1991).
[32] A. D. Martin, R. G. Roberts, W. J. Stirling, and R. S. Thorne, Phys. Lett. B **604**, 61 (2004).
[33] S. Frixione and B. Webber, J. High Energy Phys. **06**, 29 (2002).
[34] J. M. Campbell and R. K. Ellis, Phys. Rev. D **60**, 113006 (1999).
[35] A. Martin, W. Stirling, R. Thorne, and G. Watt, Eur. Phys. J. C **63**, 189 (2009).
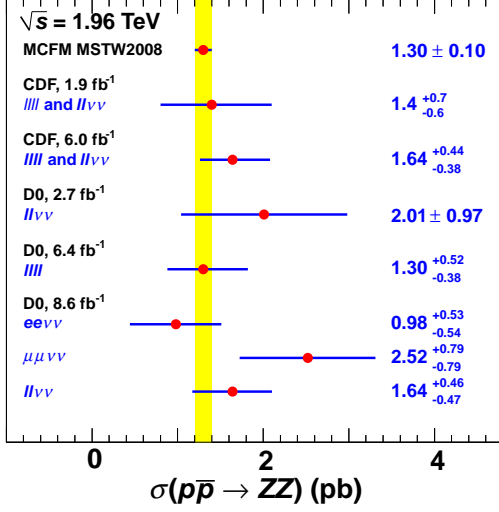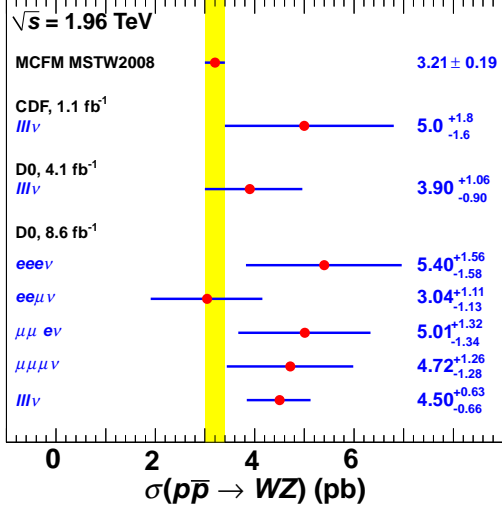
FIG. 9: Comparison of the measured ZZ and WZ cross sections with SM predictions, and with previous measurements in leptonic final states. The ZZ cross section measured by D0 in the $ZZ \rightarrow \ell^+\ell^-\ell^+\ell^-$ channel has been corrected to the same dilepton invariant mass range as considered in this analysis.